

Probing anisotropies of gravitational-wave backgrounds with a space-based interferometer III: *Reconstruction of a high-frequency skymap*

Atsushi Taruya^{1,*}

¹ *Research Center for the Early Universe (RESCEU),
School of Science, The University of Tokyo, Tokyo 113-0033, Japan*

We develop a numerical scheme to make a high-frequency skymap of gravitational-wave backgrounds (GWBs) observed via space-based interferometer. Based on the cross-correlation technique, the intensity distribution of anisotropic GWB can be directly reconstructed from the time-ordered data of cross-correlation signals, with full knowledge of detector's antenna pattern functions. We demonstrate how the planned space interferometer, LISA, can make a skymap of GWB for a specific example of anisotropic signals. At the frequency higher than the characteristic frequency $f_* = 1/(2\pi L)$, where L is the arm-length of the detector, the reconstructed skymap free from the instrumental noise potentially reaches the angular resolution up to the multipoles $\ell \sim 10$. The presence of instrumental noises degrades the angular resolution. The resultant skymap has angular resolution with multipoles $\ell \leq 6 \sim 7$ for the anisotropic signals with signal-to-noise ratio $S/N > 5$.

PACS numbers: 04.30.-w, 04.80.Nn, 95.55.Ym, 95.75.-z, 95.30.Sf

I. INTRODUCTION

The incoherent superposition of gravitational waves coming from many unresolved sources and/or diffuse-sources may form a stochastic background of gravitational waves. While such a tiny signal is in nature random, their statistical properties contain valuable cosmological information about the astrophysical phenomena and the cosmic expansion history. Potentially, the extremely early stage of the universe can be directly probed by using the gravitational-wave background (GWB), beyond the last scattering surface of cosmological microwave background.

Aiming at detecting the tiny fluctuations, several future missions of space-based interferometers have been proposed. Among these, Laser Interferometer Space Antenna (LISA) will be a first-generation space-based detector launched in the next decade ¹. The main target of LISA is the low-frequency gravitational waves of astrophysical origin around $1 \sim 10$ mHz. It is expected that large population of Galactic binaries produces a strong signal of GWB at $f \lesssim 1$ mHz [1, 2, 3]. Further, the extragalactic signals of GWB would be detected at high-frequency band [4, 5]. On the other hand, second-generation space interferometers, the DECI-hertz interferometer Gravitational wave Observatory (DECIGO) [6] and the Big-Bang Observer (BBO)² [7], have been proposed as follow-on mission of LISA. The main target of these missions is the primordial GWB produced during the inflationary epoch (e.g., [8, 9, 10, 11]). For this purpose, the observational window around $0.1 \sim 1$ Hz is considered to be suitable for direct detection. With future technology accessible to the next two decades, direct detection will be possible for the inflationary GWB with amplitude $\Omega_{\text{gw}} \sim 10^{-16}$ [12, 13, 14].

The detection of GWB in the next few decades will open a new subject of cosmology and thereby the infrastructure such as a new data analysis technique is needed to be exploited. Among various interesting problems, making a skymap of GWB is a key piece in observational cosmology. In our previous study, we have investigated the directional sensitivity of space interferometer to the anisotropy of GWB (Ref.[15], hereafter paper I). It turned out that the angular sensitivity of gravitational-wave detector to the anisotropic GWBs sensitively depends on the geometric configuration of space interferometer as well as the signal processing. Further, based on the correlation analysis, a method for direct reconstruction of GWB skymap has been exploited (Ref.[16], hereafter paper II). Employing the perturbative technique, a low-frequency skymap of GWB can be directly reconstructed (for the reconstruction in the low-frequency limit, see Ref.[17]).

The aim of the present paper is to extend our previous study to the direct reconstruction of a high-frequency skymap beyond the low-frequency approximation. We give a simple reconstruction method, in which the problem is reduced to find a solution of the linear algebraic system. While the governing linear equation often becomes

*Electronic address: ataruya@utap.phys.s.u-tokyo.ac.jp

¹ URL, <http://lisa.jpl.nasa.gov/>, <http://sci.esa.int/science-e/www/area/index.cfm?fareaid=27>

² URL, <http://universe.nasa.gov/program/bbo.html>

under-determined, with a full numerical treatment, the present scheme gives an approximate but reliable solution for skymap reconstruction. As a demonstration, we consider a specific example for the reconstruction problem using the space interferometer LISA. We show that at the high-frequency band higher than the characteristic frequency $f_* = 1/(2\pi L) \sim 9.52\text{mHz}$, the LISA can make a skymap of GWB with angular resolution up to the multipoles $\ell \sim 10$. The presence of instrumental noises significantly degrades the angular resolution and thereby the reconstructed result of the multipole coefficients for GWB skymap includes a larger error. However, with the signal-to-noise ratio $S/N > 5$, the resultant skymap has angular resolution with multipoles $\ell \leq 6 \sim 7$.

The paper is organized as follows. In Sec. II, based on the cross-correlation technique to detect the stochastic signals, we briefly review how to extract the information of anisotropies of the GWBs and present the simple reconstruction scheme, which is capable of applying to the high-frequency skymap. Several distinctions between the high-frequency and the low-frequency cases are discussed. In Sec. III, the reconstruction scheme is demonstrated in the specific model of the anisotropic GWB, i.e., Galactic white dwarf binaries. The quality of the reconstructed skymap is quantified in both the noise-free and the noisy cases. Finally, Sec. IV is devoted to the summary and the discussion.

II. METHODOLOGY

A. Map-making problem

Before addressing the reconstruction scheme, we briefly summarize how one can detect the anisotropies of GWB via space interferometer.

The planned space interferometer, LISA and also the next generation detectors DECIGO/BBO constitute several spacecrafts, each of which exchanges laser beams with the others. Combining these laser pulses, it is possible to synthesize the various output streams which are sensitive (or insensitive) to the gravitational-wave signal. In particular, technique to synthesize data streams canceling the laser frequency noise is known as time-delay interferometry (TDI), which is crucial for LISA mission ([18, 19, 20], see [21] for a review). In the present paper, signals produced by TDI technique are used to demonstrate the skymap reconstruction.

The multiple data streams constructed from specific combinations of laser pulses can be used to detect the GWBs through the correlation analysis. Suppose that one obtains the two output streams denoted by $s_I(t)$ and $s_J(t)$, the correlation analysis can be made by calculating the ensemble average $C_{IJ} \equiv \langle s_I(t)s_J(t) \rangle$. Naively, one may think that the correlation signal C_{IJ} becomes time-independent if both the signal and the instrumental noises obeys stationary random process. However, this is not entirely correct, because the sensitivity of gravitational-wave detector has specific angular response to the GWB. Further, the motion of space interferometer is inherently non-stationary. For LISA, the constellation of three space crafts orbits around the Sun with a period of one sidereal year and the orientation of the gravitational-wave detector gradually changes relative to the sky. Hence, in presence of the anisotropic GWB, the amplitude of correlation signal cannot be constant, but varies in time. This is key ingredient for reconstruction of the GWB skymap. The basic equation characterizing the non-stationarity of the correlation signal can be written in the Fourier domain as (paper I, II, [22, 23, 24, 25, 26]):

$$C_{IJ}(f, t) = \int \frac{d\Omega}{4\pi} S_h(f, \Omega) \mathcal{F}_{IJ}(f, \Omega; t), \quad (1)$$

where the correlation signal $C(f, t)$ is related with the one in the time-domain through the expression, $C_{IJ} = \int df C_{IJ}(f, t)$. The quantity S_h represents the power spectral density of GWB, which is, in general, the unknown function of the frequency and the sky position. On the other hand, the function \mathcal{F}_{IJ} is called the antenna pattern function, which characterizes the angular response of gravitational-wave detector, and the precise functional form of it is known from the configuration and the orientation of the detector (see Appendix A).

Eq. (1) implies that the luminosity distribution of GWB $S_h(f, \Omega)$ is reconstructed by deconvolving the all-sky integral of antenna pattern function from the time-series data $C_{IJ}(f, t)$. To see this more explicitly, we decompose the antenna pattern function and the luminosity distribution of GWB into spherical harmonics in a sky-fixed coordinate system:

$$S_h(|f|, \Omega) = \sum_{\ell, m} [p_{\ell m}(f)]^* Y_{\ell m}^*(\Omega), \quad \mathcal{F}_{IJ}(f, \Omega; t) = \sum_{\ell, m} a_{\ell m}(f, t) Y_{\ell m}(\Omega). \quad (2)$$

Note that the properties of spherical harmonics yield $p_{\ell m}^* = (-1)^m p_{\ell, -m}$ and $a_{\ell m}^* = (-1)^{\ell-m} a_{\ell, -m}$, where the latter property comes from $\mathcal{F}_{IJ}^*(f, \Omega; t) = \mathcal{F}_{IJ}(f, -\Omega; t)$ (paper I). Substituting (2) into (1) becomes

$$C_{IJ}(t, f) = \frac{1}{4\pi} \sum_{\ell m} a_{\ell m}(f, t) [p_{\ell m}(f)]^*. \quad (3)$$

Thus, the problem to reconstruct a GWB skymap reduces to the linear algebraic problem. That is, collecting the correlation signals measured at different times and solving the couples of linear equations, the multipole coefficient of GWB $p_{\ell m}(f)$ can be obtained under a full knowledge of time-dependent coefficients $a_{\ell m}(f, t)$.

Several important remarks should be mentioned in order. First, the accessible multipole coefficients $p_{\ell m}$ are severely restricted by the angular sensitivity of antenna pattern functions. According to paper I, the space interferometer LISA is typically sensitive to the multipole coefficients $\ell \lesssim 5$ of the anisotropic GWBs in the low-frequency regime and to the multipoles $\ell \lesssim 10$ in the high-frequency regime. Second, the above linear system is generally either over-constrained or under-determined. In the presence of the instrumental noises, this deconvolution problem tends to become under-determined system (paper II). As a consequence, exact reconstruction is no longer than possible in practice and we need to exploit an approximate method to reconstruct the GWB skymap with a limited angular resolution.

B. Reconstruction scheme

In what follows, assuming a prior knowledge of the time-dependent antenna pattern functions, we present simple reconstruction method for a GWB skymap from time-modulated correlation signals. In paper II, employing the perturbative expansion of the antenna pattern functions, reconstruction method for a low-frequency skymap has been presented. In the present paper, we especially focus on the high-frequency skymap. Here, the high-frequency means that the wavelength of the gravitational waves is comparable or shorter than the arm-length of the detector (or separation between the two detectors that produce the correlation signals), where the low-frequency approximation of the antenna pattern breaks down.

The basic strategy to make a high-frequency skymap is almost the same as in paper II. Suppose that for a given frequency f , one obtains the discrete time-series data for correlation signals as $C_{IJ}(f, t_i)$ ($i = 1, 2, \dots, N$). We then write Eq. (3) in the matrix form as:

$$\mathbf{c}(f) = \mathbf{A}(f) \cdot \mathbf{p}(f), \quad (4)$$

where the vector \mathbf{c} has N columns, each of which contain the correlation signal $C_{IJ}(f; t_i)$. The vector $\mathbf{p}(f)$ represents the unknown multipole coefficients of the GWB spectrum and in each column, we have $p_{\ell m}^*$. Thus, if one truncates the spherical harmonic expansion with the multipole ℓ_{\max} , the total number of the elements in vector $\mathbf{p}(f)$ becomes $(\ell_{\max} + 1)^2$. On the other hand, the matrix \mathbf{A} contains the multipole coefficients of antenna pattern functions and the matrix has $a_{\ell m}(f, t_i)$ in each element. With the truncation multipole ℓ_{\max} , the quantity \mathbf{A} forms a $(\ell_{\max} + 1)^2 \times N$ matrix.

As mentioned in previous subsection, the linear system (4) tends to become an under-determined system, i.e., $(\ell_{\max} + 1)^2 > N$, and \mathbf{A} is generally a rectangular matrix. In such a situation, unique and exact solution of the linear equations (4) cannot be obtained. In paper II, approximate treatment to solve the equations (4) has been presented based on the idea of least-squares method. In linear system, this approximation is expressed in the following form:

$$\mathbf{p}_{\text{approx}}(f) = \mathbf{A}^+(f) \cdot \mathbf{c}(f), \quad (5)$$

where \mathbf{A}^+ is the pseudo-inverse matrix of Moore-Penrose type. The explicit expression is determined from the singular-value decomposition of the matrix \mathbf{A} , i.e., $\mathbf{A} = U^\dagger \cdot \text{diag}[w_i] \cdot V$. Then we have (e.g., [27])

$$\mathbf{A}^+ = V^\dagger \cdot \text{diag}[w_i^{-1}] \cdot U. \quad (6)$$

In paper II, owing to the perturbative expansion, the multipole coefficients of antenna pattern function can be computed analytically up to the multipole $\ell = 5$ and the matrix \mathbf{A} is constructed in an analytic manner. It is shown that the least-squares solution (5) provides an accurate approximation for multipole moments $p_{\ell m}$ in both overdetermined and under-determined cases.

In the high-frequency regime which we are interested in, the angular resolution of antenna pattern function can be improved and one expects that detectable multipole coefficients increase compared to those of the low-frequency skymap. As a price, it is no longer possible to compute the multipole coefficients $a_{\ell m}$ analytically and the spherical harmonic expansion of antenna pattern function becomes a fully numerical task. In the present paper, we use the Fortran package, SPHEREPACK 3.1 [28], to compute the time-dependent coefficients $a_{\ell m}$. With a full numerical treatment to evaluate Eq. (5), the reliability of the methodology will be tested in a simple reconstruction problem (Sec. III).

In principle, the methodology presented in paper II can work well even in the map-making problem of the high-frequency GWBs. Nonetheless, to further reduce the numerical error, the least-squares method (5) may be applied

by imposing the reality condition of the GWB intensity map, i.e., $p_{\ell m}(f) = (-1)^m p_{\ell, -m}^*(f)$. To do this, we introduce real quantities $q_{\ell m}$ and $r_{\ell m}$ and divide the multipole coefficient $p_{\ell m}$ into the real and the imaginary parts as

$$\begin{aligned} p_{\ell m} &= q_{\ell m} + i r_{\ell m}, \\ p_{\ell, -m} &= (-1)^m \{q_{\ell m} - i r_{\ell m}\} \end{aligned}$$

for $m > 0$ and

$$p_{\ell, 0} = q_{\ell 0}.$$

Then, Eq.(3) is rewritten with

$$\begin{aligned} C_{IJ}(f; t) &= \frac{1}{4\pi} \sum_{\ell=0} \left[a_{\ell 0} q_{\ell 0} + \sum_{m=1}^{\ell} \{a_{\ell m} + (-1)^m a_{\ell, -m}\} q_{\ell m} - i \sum_{m=1}^{\ell} \{a_{\ell m} - (-1)^m a_{\ell, -m}\} r_{\ell m} \right] \\ &= \frac{1}{4\pi} \sum_{\ell=0} \vec{a}_{\ell}(f; t) \cdot \vec{p}_{\ell}(f), \end{aligned} \quad (7)$$

where the vectors \vec{a}_{ℓ} and \vec{p}_{ℓ} have the $(2\ell + 1)$ columns, whose explicit expressions are

$$\vec{a}_{\ell} = \begin{pmatrix} a_{\ell 0} \\ \vdots \\ a_{\ell m} + (-1)^m a_{\ell, -m} \\ \vdots \\ \vdots \\ -i \{a_{\ell m} - (-1)^m a_{\ell, -m}\} \\ \vdots \end{pmatrix}, \quad \vec{p}_{\ell} = \begin{pmatrix} q_{\ell 0} \\ \vdots \\ q_{\ell m} \\ \vdots \\ \vdots \\ r_{\ell m} \\ \vdots \end{pmatrix}, \quad (8)$$

where m runs from 1 to ℓ . Hence, truncating the summation of ℓ by ℓ_{\max} and dividing the time-ordered signals into the N subsections, the matrix \mathbf{A} and the vector \mathbf{p} can be written explicitly

$$\mathbf{A} = \frac{1}{4\pi} \begin{pmatrix} \vec{a}_0(t_1) & \cdots & \vec{a}_{\ell}(t_1) & \cdots & \vec{a}_{\ell_{\max}}(t_1) \\ \vdots & \ddots & \vdots & \ddots & \vdots \\ \vec{a}_0(t_N) & \cdots & \vec{a}_{\ell}(t_N) & \cdots & \vec{a}_{\ell_{\max}}(t_N) \end{pmatrix}, \quad \mathbf{p} = \begin{pmatrix} \vec{p}_0 \\ \vdots \\ \vec{p}_{\ell_{\max}} \end{pmatrix}. \quad (9)$$

For a reliable numerical calculation, we further divide the matrix \mathbf{A} in Eq. (9) into the real and the imaginary parts and apply the least-squares approximation (5) to the linear system (4).

III. DEMONSTRATION

In this section, general reconstruction method presented in previous section is demonstrated in the case of LISA detector and the map-making capability is examined for a specific example of anisotropic GWB source.

It is expected that the low-frequency band of LISA have a strong anisotropic signals of GWB by the Galactic population of unresolved binaries. On the other hand, GWBs of high-frequency regime could be dominated by the extragalactic origin, which mainly comes from the cosmological population of white dwarf binaries [4, 5]. While the signal produced by them would reach the detectable level of LISA sensitivity, it is uncertain whether the strong anisotropic component exists or not. In this paper, just for illustrative purpose, we consider the Galactic GWB as a high-frequency source of GWB and try to reconstruct the intensity distribution of GWB.

Fig. 1 shows the projected skymap of Galactic GWB. Here, we use the simple model of Galactic GWB described in paper II (see also [26]), in which we assumed that the intensity distribution of GWB just traces the Galactic stellar distribution observed via infrared photometry [29]³. The intensity distribution shown in Fig. 1 has disk-like structure

³ To be precise, the Galactic stellar distribution is modeled by the fitting function given in Ref.[29], which consists of the triaxial bulge and the disk components.

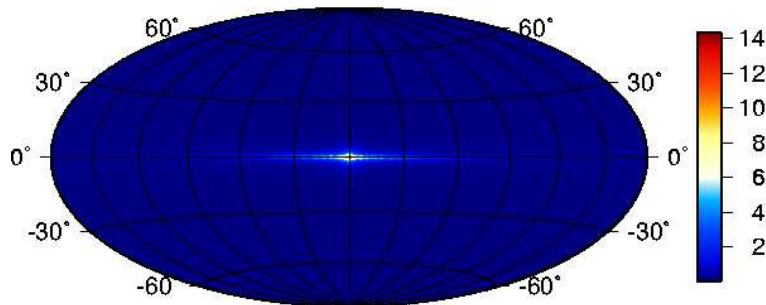


FIG. 1: Full resolution skymap for the simple model of Galactic GWB (paper II, [26]). The intensity distribution $S_h(f, \Omega) = P(\Omega)$ is depicted in the Galactic coordinate system. Here, the all-sky integral of intensity distribution is normalized to unity, i.e., $\int d\Omega P(\Omega) = 1$.

with a strong peak at Galactic center. Spherical harmonic analysis of GWB skymap reveals that the dominant contribution to the intensity distribution comes from the lower multipoles with $\ell \lesssim 4$, but the contribution from the higher multipoles still remains significant. Even at the multipole $\ell \sim 15$, it possesses the 10% power relative to the monopole component (see Table III and Fig. 12 in paper II). In this sense, it is a good exercise to diagnose the map-making capability of present reconstruction scheme.

As we mentioned in Sec. II A, signal processing technique of LISA is called the TDI, which produces the various output signals canceling the laser frequency noise by combining the time-delayed six laser pulses. Among these, optimal TDI signals referred to as the A , E and T variables are especially suitable for the detection of GWB via the correlation analysis, because these outputs are basically free from the noise correlation [30, 31]. Here, we use the optimal TDIs to produce the correlation signals. The response functions for these variables are presented in the equal armlength case in Appendix A. For the reconstruction of a high-frequency skymap, the cross-correlation signals AE , AT and ET can be the most sensitive signals of GWB and the reconstructed skymap improves the angular resolution up to the multipoles $\ell \sim 8 - 10$ around the frequencies $f \sim 2 - 10f_*$, where the characteristic frequency of LISA is given by $f_* = 1/(2\pi L) \simeq 9.52\text{mHz}$.

In what follows, specifically focusing on the frequency $f = 3f_* \simeq 28.6\text{mHz}$, we present the reconstruction results separately in idealistically noise-free case (Sec. III A) and in realistic case taking account of the instrumental noises (Sec. III B).

A. Noise-free case

Fig. 2 shows the intensity distribution of reconstructed skymap in the Galactic coordinate system. To obtain the skymap, we first create the annual modulation data of correlation signals $C_{AE}(f; t)$, $C_{AT}(f; t)$ and $C_{ET}(f; t)$ by convolving the original skymap $S_h(f, \Omega) = P(\Omega)$ with antenna pattern functions in the ecliptic coordinate system. Here the all-sky integral of $P(\Omega)$ is normalized to unity, i.e., $\int d\Omega P(\Omega) = 1$. Dividing the one-year data of correlation signals into the 32 sections ($N = 32$), the vector \mathbf{c} is then constructed. Combining it with the pseudo-inverse matrix of \mathbf{A} , we evaluate the expression (5). The resultant least-squares solution of $p_{\ell m}$ is given in the ecliptic frame and we finally transform it into the skymap in the Galactic coordinate system. Note that in step calculating the matrix \mathbf{A} , the SPHEREPACK 3.1 package was used to compute the spherical harmonic coefficients of time-dependent antenna pattern functions and the multipoles higher than $\ell = 17$ were discarded (i.e., $\ell_{\max} = 16$).

The reconstruction result in Fig. 2 shows that due to the incomplete reconstruction, the total intensity diminishes and the distribution is coarse-grained, together with fake pattern. Nevertheless, the disk-like structure of the intensity distribution is clearly seen. Compared to the result in the low-frequency band (paper II), the angular resolution is greatly improved.

It should be noticed that the present reconstruction result crucially depends on the additional parameter, i.e., the cutoff of singular values of the matrix \mathbf{A} , which we call w_{cut} . For a given w_{cut} , the pseudo-inverse matrix A^+ was constructed based on the expression (6) using the singular-values larger than w_{cut} . In Fig. 2, we specifically set the cutoff parameter w_{cut} to 10^{-7} . The cutoff value directly affects the resolution of reconstructed skymap. To show the significance of this, in Fig. 3, reconstruction results of skymap with various cutoff are plotted. Clearly, larger cutoff value makes the angular resolution of skymap worse. It seems favorable to use the small value of w_{cut} . However, as indicated in the expression (6), the result using the small singular-value tends to be sensitively affected by the errors associated with numerical computation of pseudo-inverse matrix and/or the instrumental noises. Hence, we need to

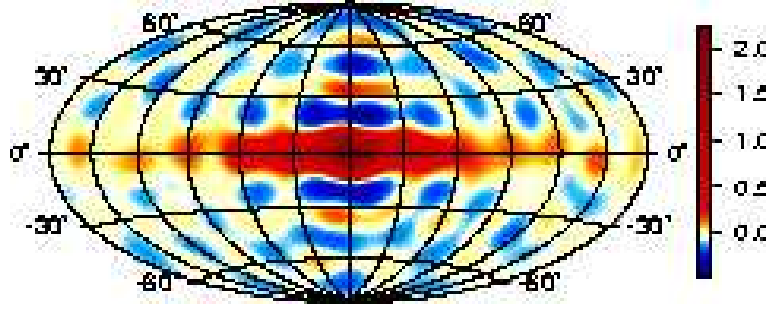


FIG. 2: Reconstructed skymap at the frequency $f = 3f_* \simeq 28.6\text{mHz}$ in the absence of instrumental noises. The cutoff parameter of singular values w_{cut} is set to 10^{-7} .

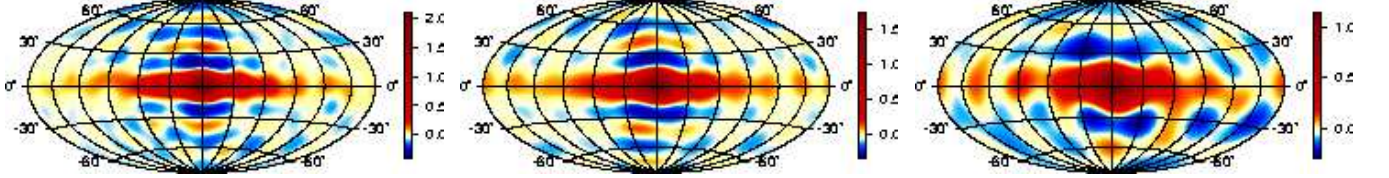


FIG. 3: Dependence of the reconstructed results on the cutoff parameter of singular values in absence of instrumental noises: $w_{\text{cut}} = 10^{-6}$ (left), 10^{-4} (middle) and 10^{-2} (right).

seek an optimal value of w_{cut} to get a better reconstruction result. This will be discussed in next subsection.

Now, we wish to quantify the quality of the reconstructed skymap and discuss the validity of present reconstruction scheme. To do this, we introduce the correlation parameter defined by

$$r_{\text{corr}}(\ell_{\text{cut}}) \equiv \frac{\langle S_h^{(\text{true})}(\boldsymbol{\Omega}; \ell_{\text{cut}}) | S_h^{(\text{reconst})}(\boldsymbol{\Omega}) \rangle}{\left[\langle S_h^{(\text{true})}(\boldsymbol{\Omega}; \ell_{\text{cut}}) | S_h^{(\text{true})}(\boldsymbol{\Omega}; \ell_{\text{cut}}) \rangle \langle S_h^{(\text{reconst})}(\boldsymbol{\Omega}) | S_h^{(\text{reconst})}(\boldsymbol{\Omega}) \rangle \right]^{1/2}}, \quad (10)$$

where the operation $\langle A|B \rangle$ for the real functions $A(\boldsymbol{\Omega}) = \sum_{\ell m} a_{\ell m} Y_{\ell m}$ and $B(\boldsymbol{\Omega}) = \sum_{\ell m} b_{\ell m} Y_{\ell m}$ means

$$\langle A|B \rangle \equiv \int d\boldsymbol{\Omega} A(\boldsymbol{\Omega})B(\boldsymbol{\Omega}) = \frac{1}{2} \sum_{\ell, m} (a_{\ell m}^* b_{\ell m} + a_{\ell m} b_{\ell m}^*). \quad (11)$$

In the expression (10), while the quantity $S_h^{(\text{reconst})}$ represents the reconstructed skymap from the least-squares solution (5), the function $S_h^{(\text{true})}$ is the skymap of the true intensity distribution dropping the higher multipole moments with $\ell > \ell_{\text{cut}}$. To be precise, this is defined by

$$S_h^{(\text{true})}(\boldsymbol{\Omega}; \ell_{\text{cut}}) = \sum_{\ell=0}^{\ell_{\text{cut}}} \sum_{m=-\ell}^{\ell} p_{\ell m}^{(\text{true})} Y_{\ell m}(\boldsymbol{\Omega}). \quad (12)$$

The correlation parameter $r_{\text{corr}}(\ell_{\text{cut}})$ quantifies the degree of similarity between the reconstructed skymap and the true skymap subtracting the higher multipoles. Hence, evaluating $r_{\text{corr}}(\ell_{\text{cut}})$, one can characterize the angular resolution of the GWB skymap. In addition to this, we also introduce the averaged fractional error for the multipole coefficients $p_{\ell m}$, $\text{Err}[p_{\ell m}]$, given by

$$\text{Err}[p_{\ell m}] \equiv \left\{ \frac{1}{2\ell + 1} \sum_{m=-\ell}^{\ell} \left| \frac{p_{\ell m}^{(\text{reconst})} - p_{\ell m}^{(\text{true})}}{p_{\ell m}^{(\text{true})}} \right|^2 \right\}^{1/2}, \quad (13)$$

which quantifies the accuracy of the determination of multipole coefficients. With the two quantities $r_{\text{corr}}(\ell_{\text{cut}})$ and $\text{Err}[p_{\ell m}]$, the quality and the accuracy of the reconstructed skymap can be quantified.

Left panel of Fig. 4 shows the correlation parameters for the reconstructed skymap with various cutoff values w_{cut} . For a fixed value w_{cut} , the correlation parameter as function of truncation multipole ℓ_{cut} has a single peak

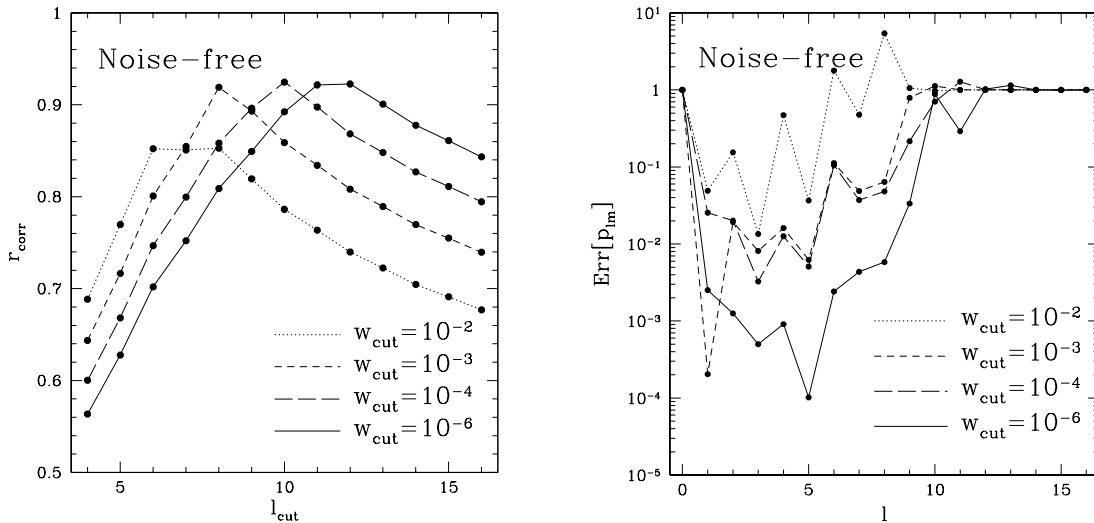


FIG. 4: *Left*: Cross-correlation parameters r_{corr} as function of cutoff multipole l_{cut} . *Right*: averaged fractional error of $p_{\ell m}$, $\text{Err}[p_{\ell m}]$ as function of multipole, l (see Eq.(13)).

and the peak value is typically $r_{\text{corr}} \sim 0.92$. As decreasing the cutoff value w_{cut} , the location of peak tends to be shifted to a larger l_{cut} , indicating that the angular resolution becomes improved. For small cutoff value $w_{\text{cut}} = 10^{-6}$, reconstructed skymap is qualitatively similar to the true skymap dropping the higher multipoles $l > 12$.

Right panel of Fig. 4 shows the root-mean-square value of the averaged fractional error of $p_{\ell m}$, i.e., $\text{Err}[p_{\ell m}]$. As anticipated from left panel, the smaller value of w_{cut} tends to decrease the errors in each multipole coefficient. However, due to the low-resolution of the antenna pattern function, the reconstructed results for higher multipoles $l > 10$ become almost vanishing. As a result, the fractional error $\text{Err}[p_{\ell m}]$ of $l > 10$ approaches unity. It should be noticed that the fractional error also becomes unity for the monopole moment of GWB signal. This reflects the important properties that the cross-correlation of optimal TDI variables are *generally blind* to the monopole intensity for the *AT* and *ET* signals and also to the dipole anisotropy for the *AE* signal. It has been shown in paper I that these features generally hold irrespective of the observed frequency band. In this respect, map-making issue with LISA would be problematic in determining of the monopole intensity. Apart from this, right panel of Fig. 4 implies that the present reconstruction scheme has a potential to provide a precise determination of multipoles. With the cutoff value $w_{\text{cut}} = 10^{-6}$, the accuracy can reach less than a few percent level. Of course, these are the outcome based on the idealistic situation free from the instrumental noises. In next subsection, the significance of the instrumental noises on the map-making problem will be clarified.

B. Noisy case

In reality, the instrumental noises are additively mixed into the time-series data of gravitational-wave signals. While the cross-correlation variables *AE*, *AT* and *ET* themselves are free from the noise correlation, the correlation analysis with finite number of samples is inherently affected by the statistical fluctuations, among which the instrumental noises becomes the most dominant component in the weak-signal case. To discuss their influences on the map-making problem, we first quantify the signal-to-noise ratio for the stochastic GWB. Based on the cross-correlation statistic with a suitable filter function, the signal-to-noise (S/N) ratio for the stochastic GWB in the specific frequency interval $f - \Delta f/2 \sim f + \Delta f/2$ is defined by (e.g., [14, 32]):

$$\left(\frac{S}{N}\right) \equiv (T_{\text{obs}} \Delta f)^{1/2} \left[\sum_{(I,J)} \frac{\overline{|C_{IJ}(f;t)|^2}}{N_I(f)N_J(f)} \right]^{1/2}; \quad \overline{|C_{IJ}(f;t)|^2} \equiv \frac{1}{T_{\text{orbit}}} \int_0^{T_{\text{orbit}}} dt |C_{IJ}(f;t)|^2, \quad (14)$$

where the summation (I, J) represents the sum over the whole cross-correlation data (i.e., *AE*, *AT* and *ET*). The quantities T_{orbit} and T_{obs} respectively denote the orbital period of LISA corresponding to the one year and the total observation time longer than the orbital period. Below, we specifically set the parameters to $T_{\text{obs}} = 10^8 \text{sec}$ and $\Delta f = 10^{-3} \text{Hz}$. The function $N_I(f)$ represents the noise spectral density for the output data *I*. The explicit functional

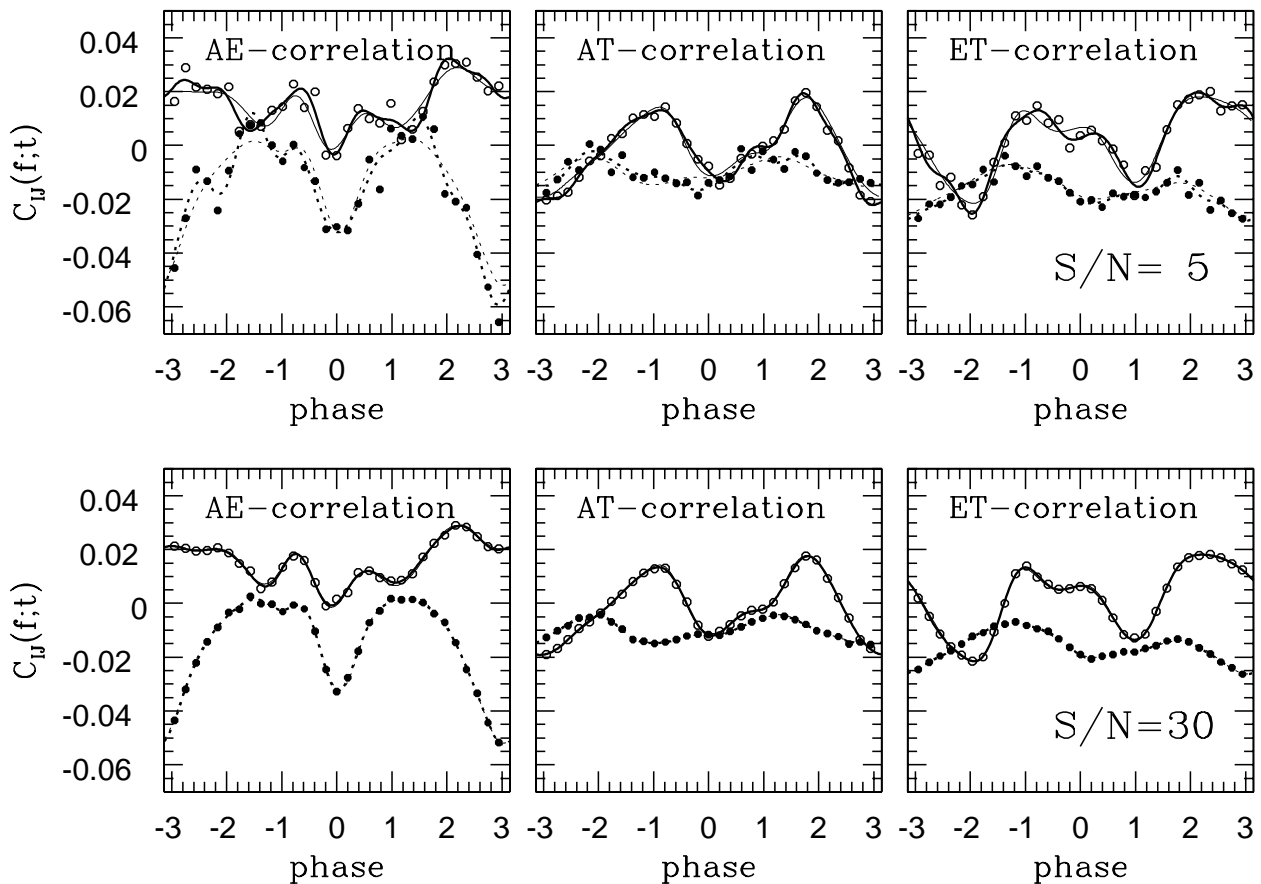


FIG. 5: Annual modulation data of cross-correlation signals C_{AE} (left), C_{AT} (middle) and C_{ET} (right) measured at the frequency $f = 3f_* \simeq 28.6\text{mHz}$. Top and bottom panels show the results with signal-to-noise ratio $S/N=5$ and 30, respectively. In each panel, filled and open circles represent the real and the imaginary parts of the noisy signals \hat{C}_{IJ} generated according to Eq. (15). While the continuous thin lines indicates the correlation signals free from the detector noise, thick lines indicate the fitted result of the noisy signals to the harmonic functions (16).

form of the noise spectrum is given in Appendix A, together with the specific parameters of the proof mass and the optical-path noises for LISA.

We are specifically concerned with the qualitative change of the reconstructed skymap in the presence of instrumental noises. For this purpose, rather than performing a large-scale extensive simulation that mimics a realistic signal processing [33, 34, 35], we here perform a very simple simulation in which the random noises are added by hand to the (noise-free) correlation signals computed in previous subsection. To be precise, for i -th sub-sectional data of the totally $N = 32$ correlation signals C_{IJ} , we generate the time-series random data \hat{C}_{IJ} as

$$\hat{C}_{IJ}(f; t_i) = C_{IJ}(f; t_i) + \left\{ \frac{N_I(f)N_J(f)}{(T_{\text{obs}}/N) \Delta f} \right\}^{1/2} \frac{\hat{\xi}_1 + i\hat{\xi}_2}{\sqrt{2}}, \quad (i = 1, \dots, N) \quad (15)$$

where the variables $\hat{\xi}_i$ are the Gaussian random variables with zero mean and unit variance, i.e., $\langle \hat{\xi}_i \rangle = 0$ and $\langle \hat{\xi}_i^2 \rangle = 1$. In the above expression, the first term in right-hand-side is the theoretical time-modulation signals used in previous subsection, where the amplitude of GWB signal, $S_h(f, \boldsymbol{\Omega}) = A \cdot P(\boldsymbol{\Omega})$. On the other hand, the second term represents the randomness arising from the instrumental noises, whose amplitude is estimated based on the S/N ratio in weak-signal limit.

Fig. 5 shows the time-series data of cross-correlation signals for Galactic GWB in the case of $S/N=5$ (top) and $S/N=30$ (bottom). The open and the filled circles represent the real and the imaginary parts of the noisy data \hat{C}_{IJ} , respectively. Note that in plotting the data, we set $A = 1$ so that the all-sky integral of GWB spectrum is normalized to unity and the amplitude of the random noises is appropriately rescaled according to the S/N values. As it is clear, direct use of the raw noisy data makes the quality of the reconstructed image worse. Hence, we tried to fit the noisy

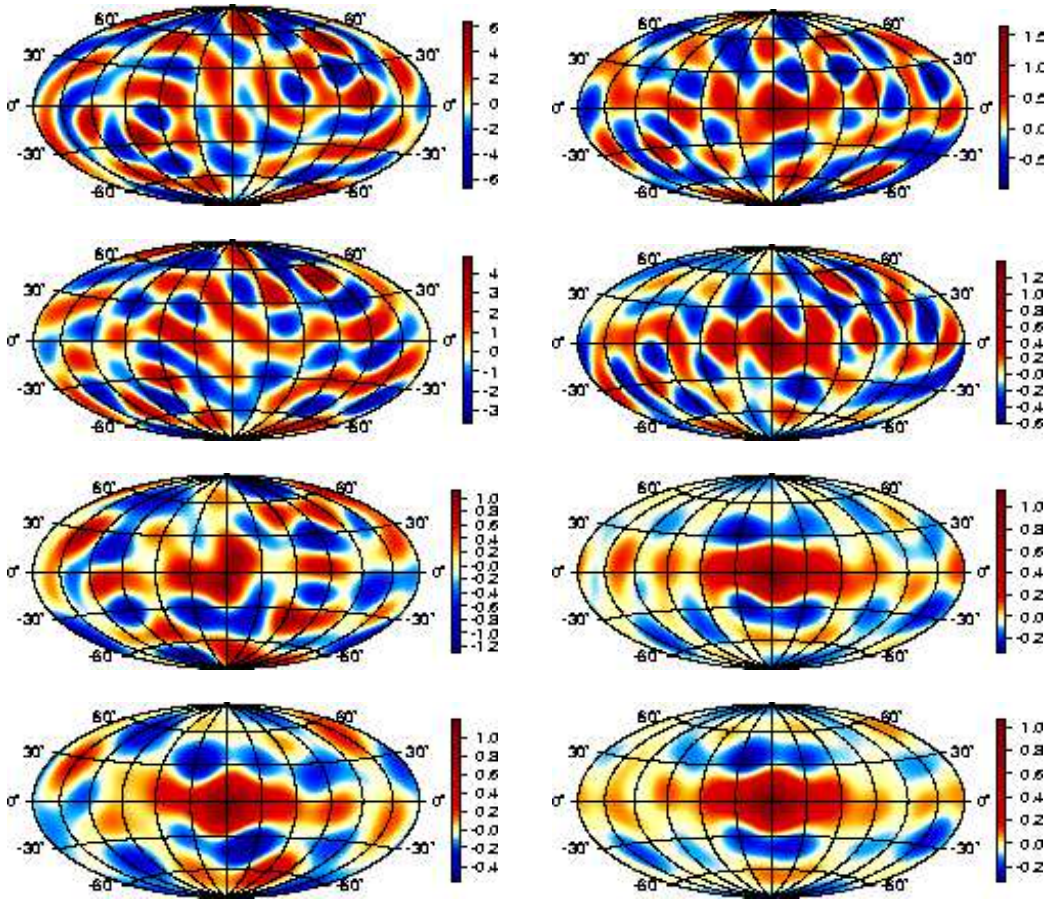


FIG. 6: Reconstructed skymap from the noisy data (see Fig. 5). Left and right panels respectively show the results from the $S/N=5$ and 30 noisy data. From top to bottom, the cutoff parameter of singular values were set to $w_{\text{cut}} = 10^{-3}$, 5×10^{-3} , 10^{-2} and 5×10^{-2} .

data \hat{C}_{IJ} to the harmonic functions $f_{IJ}(t)$:

$$f_{IJ}(t) = \sum_{k=-k_{\text{max}}}^{k_{\text{max}}} c_k e^{ik\omega_{\text{orbit}} t}; \quad \omega_{\text{orbit}} = 2\pi/T_{\text{orbit}}. \quad (16)$$

The resultant fitting functions were then used to perform the reconstruction scheme. In Fig. 5, the thick-solid and the thick-dashed lines are the results fitted to the harmonic function (16) with $k_{\text{max}} = 8$. For comparison, we also plot the continuous thin lines as the noise-free correlation signals.

Fig. 6 shows the reconstructed results from the noisy data for the various cutoff parameters of the singular-values, w_{cut} : $w_{\text{cut}} = 10^{-3}$, 5×10^{-3} , 10^{-2} and 5×10^{-2} from top to bottom. The left panel plots the results in the $S/N=5$ cases, while the right panel shows the skymap in the $S/N=30$ cases. The skymap with small cutoff value $w_{\text{cut}} = 10^{-3}$ is affected by the instrumental noises and the resultant intensity map show featureless fake patterns. As increasing the cutoff parameter, fake intensity pattern gradually disappears and the strong intensity peak seen in the original GWB map becomes prominent. The quality of the resultant skymap with large w_{cut} depends on the signal-to-noise ratio, S/N . For the cutoff parameter $w_{\text{cut}} = 10^{-2}$, the resultant skymap in the $S/N=30$ case is very similar to the one in the noise-free result with $w_{\text{cut}} = 10^{-2}$ (right panel of Fig. 3), while the fake intensity image is still dominant in the $S/N=5$ case.

The influence of instrumental noises shown in Fig. 6 may be easily deduced from the expression (5) with (6). In the presence of the noise, the vector \mathbf{c} which represents the correlation signals additionally contains the noise term \mathbf{n} and one can write it as $\mathbf{c} = \mathbf{A} \cdot \mathbf{p} + \mathbf{n}$. Then, the least-squares approximation (5) leads to the unwanted term $\mathbf{A}^+ \cdot \mathbf{n}$. Since the pseudo-inverse matrix \mathbf{A}^+ contains the reciprocal of the singular values, $\{w_i^{-1}\}$, this additional contribution can become dominant and affect the final reconstructed result unless introducing a larger cutoff value w_{cut} . Therefore, in order to reduce the influence of the noise term, the cutoff parameter should be, at least, set to $\sim (S/N)^{-1}$.

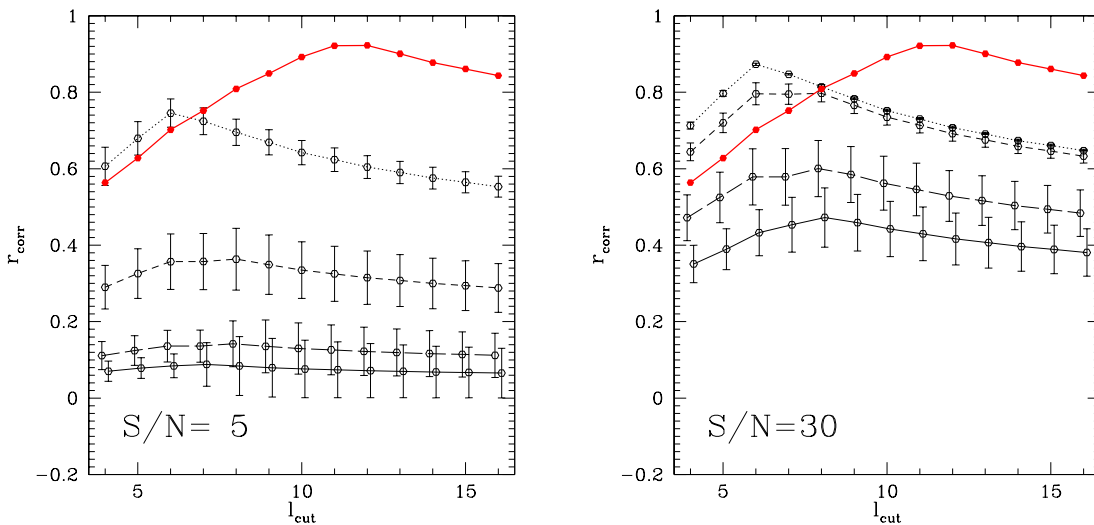


FIG. 7: Cross-correlation parameters of reconstructed skymap in presence of the instrumental noises with $S/N=5$ (left) and $S/N=30$ (right). In both panels, the cutoff parameters of the singular-values of the matrix \mathbf{A} were set to $w_{\text{cut}} = 10^{-3}$ (solid), 5×10^{-3} (long-dashed), 10^{-2} (short-dashed) and 5×10^{-2} (dotted), from bottom to top. The error bars are estimated from the sample variation among 100 realizations. For comparison, the cross-correlation parameter in the noise-free case ($w_{\text{cut}} = 10^{-6}$) is also plotted in thick solid line.

In Fig. 7, quality of the reconstructed skymap is quantified by evaluating the correlation parameters r_{corr} . Also, the averaged fractional errors $\text{Err}[p_{\ell m}]$ are computed and are presented in Fig. 8 for various cutoff values. In both figures, the error bars indicate the 1σ variation among 100 realizations. As anticipated from Fig. 6, the quality of final skymap is significantly degraded in the case of the low S/N data. The result with a smaller cutoff value w_{cut} has a little correlation with the true skymap due to many fake patterns, which is mainly attributed to the errors in the higher multipoles $\ell > 8$. For the high-signal-to-noise ratio $S/N=30$, the situation is somehow improved. With a cutoff value around $w_{\text{cut}} \sim (S/N)^{-1}$, the quality of reconstructed image becomes similar to the true map with $\ell \lesssim 6-7$. The fractional error in each multipole coefficient reaches $\sim 10\%$, although it seems still miserable compared with the noise-free result.

Finally, accuracy of the reconstructed multipoles achieved with a given signal-to-noise ratio S/N is shown in Fig. 9. Except for $S/N=100$, the cutoff value was all fixed to $w_{\text{cut}} = 5 \times 10^{-2}$. For high signal-to-noise ratio $S/N=100$, the accuracy is further improved adopting the small cutoff parameter, $w_{\text{cut}} = 5 \times 10^{-3}$. In Fig. 9, apart from the monopole moment and the higher multipoles of $\ell > 8$, there exist some multipoles that are still difficult to determine. Recalling from the similar trend found in the noise-free case (right panel of Fig. 4), the non-uniformity of the accuracies might be attributed to the angular response of the antenna pattern functions at the frequency $f = 3f_*$, not the character of the specific model of anisotropic GWB. This implies that the multi-frequency data analysis is important for the accurate determination of the multipole moments $p_{\ell m}$. Anyway, the quantitative estimation of $p_{\ell m}$ at few percent level seems very difficult even when $S/N=100$. This means that in contrast to the low-frequency case, the present reconstruction method might not be so powerful to determine each multipole moment of high-frequency skymap, but should be rather helpful to study the all-sky distribution of anisotropic GWBs in bird-eye view.

IV. SUMMARY & DISCUSSION

In this paper, we have discussed the reconstruction of a high-frequency skymap of gravitational-wave backgrounds with a space-based interferometer. Owing to the cross-correlation technique, we present a simple numerical scheme to reconstruct a skymap of anisotropic stochastic signals. While the methodology presented here is basically the same one as described in paper II, i.e., least-squares solution of linear algebraic system, there are several distinctions in the reconstruction of the high-frequency skymap. First of all, the antenna pattern function becomes complicated and the analytic treatment based on the perturbative expansion of antenna pattern function is intractable. Hence, a full numerical treatment to reconstruct the higher multipole moments is necessary. On the other hand, the sensitivity to the high-frequency signals is improved and no multi-frequency data is needed for the reconstruction of GWB skymap. As a result, the skymap with LISA demonstrated in the Galactic GWB case yields a better angular resolution up to the multipoles $\ell \sim 10$ in the absence of the instrumental noises. The presence of noises degrades the angular

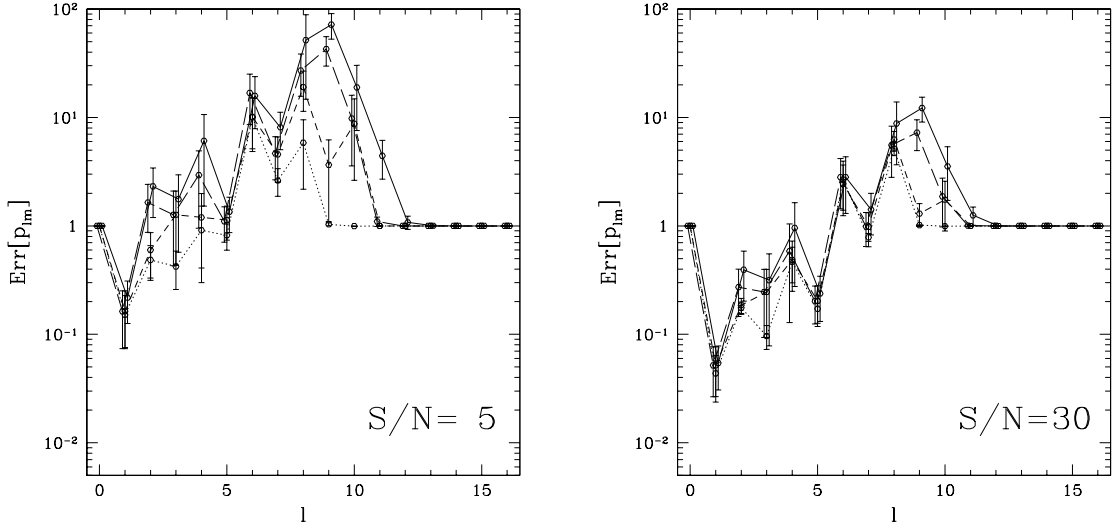


FIG. 8: Averaged fractional error of $p_{\ell m}$, $\text{Err}[p_{\ell m}]$ as function of ℓ in the presence of noises. The left and right panels represent the results with $S/N=5$ and 30 , respectively. In both panels, the cutoff parameters w_{cut} were chosen as 10^{-3} (*solid*), 5×10^{-3} (*long-dashed*), 10^{-2} (*short-dashed*) and 5×10^{-2} (*dotted*). The error bars indicate the 1σ variation among 100 realizations.

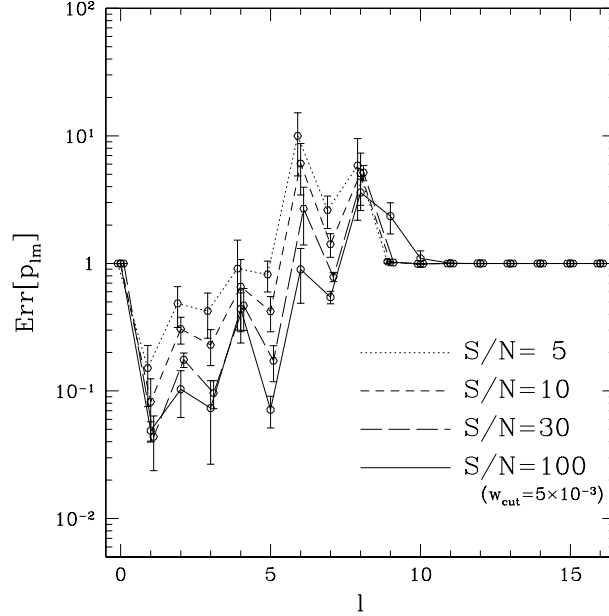


FIG. 9: Same as in Fig. 8, but the dependence of signal-to-noise ratio is shown. The solid, long-dashed, short-dashed and dotted lines respectively show the results with $S/N=100$, 30 , 10 and 5 . In each case, except for $S/N=100$, the cutoff parameter w_{cut} was set to 5×10^{-2} . In the case of the high signal-to-noise ratio $S/N=100$, fractional error can be further reduced if one adopt a smaller cutoff value. In this plot, the result with $w_{\text{cut}} = 5 \times 10^{-3}$ is shown.

resolution and the multipole coefficients for GWB skymap includes a larger error. However, with the signal-to-noise ratio $S/N > 5$, the resultant skymap has angular resolution with multipoles $\ell \leq 6 \sim 7$, which gives a better quality compared to the one achieved by the low-frequency skymap.

Since the methodology presented here is still very primitive, there would be several extensions to improve the angular resolution of reconstructed skymap. Perhaps, one naive approach is the combination of the multi-frequency data set. With the multiple data, one effectively increases the signal-to-noise ratio. Also, the directional information for anisotropic signals would be obtained additionally, through the frequency-dependent angular response of antenna pattern functions. Another possible approach is to combine the parametric models of GWB distribution characterized by the finite number of parameters and to determine these parameters. With fewer parameter set, the present

methodology tightly constrains the model parameters.

The reconstructed skymap obtained from the present scheme may be regarded as the first step of the synthesis imaging processing, like a *dirty map* in radio astronomy [36]. Under a priori information about the source distribution and the reasonable assumptions, it would be CLEANed by using the iterative deconvolution algorithm (see Ref.[37] for the application of CLEAN algorithm to the data analysis of gravitational waves). That is, with the compact GWB distribution coming from the nearby sources, one can create the synthesized GWB map convolving with the antenna pattern functions. We then subtract each compact component from the dirty map and repeat the procedure iteratively until all significant source structure has been removed. A CLEAN map is finally obtained from the residual intensity distribution by adding the removed GWB components with suitably smoothed sampling function. This CLEAN map would be useful and helpful to discriminate the GWBs of nearby origin and cosmological origin and even to identify the specific GWB signals.

Finally, the map-making problem considered in the paper is related to the tomographic reconstruction technique to resolve the distribution of the binaries [38]. While the present technique only relies on the amplitude of the signals, the tomographic approach fully takes account of the phase information. As a result, the angular resolution is greatly improved and the identification of signals becomes efficient even in the crowded samples. This may be a hint to improve the angular resolution of GWB skymap.

Acknowledgments

We thank Hideaki Kudoh, Yoshiaki Himemoto, Takashi Hiramatsu and Shun Saito for discussions and comments. We also thank Naoki Seto for careful reading of the manuscript and discussions. This work was supported by a Grant-in-Aid for Scientific Research from the Japan Society for the Promotion of Science (No. 18740132).

APPENDIX A: ANTENNA PATTERN FUNCTIONS AND INSTRUMENTAL NOISES

Here, we give an explicit expressions for antenna pattern functions for LISA used in the main text. First recall the definition of the antenna pattern function (paper I, II, [24]):

$$\begin{aligned} \mathcal{F}_{IJ}(f, \boldsymbol{\Omega}; t) &= e^{i2\pi f \boldsymbol{\Omega} \cdot (\mathbf{x}_I - \mathbf{x}_J)} \sum_{A=+, \times} F_I^{A*}(\boldsymbol{\Omega}, f; t) F_J^A(\boldsymbol{\Omega}, f; t) \\ F_I^A(\boldsymbol{\Omega}, f; t) &= \mathbf{D}_I(\boldsymbol{\Omega}, f; t) : \mathbf{e}^A(\boldsymbol{\Omega}), \end{aligned} \quad (\text{A1})$$

where \mathbf{e}^A is the polarization tensor for GWB and \mathbf{D}_I is the detector tensor for each output signal, to which we specifically adopt the optimal TDI variables A , E and T . The advantage of using the optimal TDIs in the cross-correlation analysis is that the noise spectra for cross-correlation data becomes exactly vanishing [30, 31]. These variables are simply realized by combining the three Sagnac signals called S_1 , S_2 and S_3 (often quoted as α , β and γ in the literature):

$$\begin{aligned} \mathbf{D}_A &= \frac{1}{\sqrt{2}}(\mathbf{D}_{S_3} - \mathbf{D}_{S_1}), \\ \mathbf{D}_E &= \frac{1}{\sqrt{6}}(\mathbf{D}_{S_1} - 2\mathbf{D}_{S_2} + \mathbf{D}_{S_3}), \\ \mathbf{D}_T &= \frac{1}{\sqrt{3}}(\mathbf{D}_{S_1} + \mathbf{D}_{S_2} + \mathbf{D}_{S_3}). \end{aligned} \quad (\text{A2})$$

The detector tensor for Sagnac signals can be obtained from the time-delayed combinations of one-way Doppler tracking calculations for optical-path length [15, 39, 40]. For example, the Sagnac signal S_1 measures the phase difference between two laser beams received at space craft 1, each of which travels around the LISA array in clockwise or counter-clockwise direction. Then, in the equal-arm length limit, the detector tensor for S_1 becomes

$$\begin{aligned} \mathbf{D}_{S_1}(\boldsymbol{\Omega}, f; t) &= \frac{1}{2} [\{\mathbf{a}(\mathbf{t}) \otimes \mathbf{a}(\mathbf{t})\} \mathcal{T}_a(\boldsymbol{\Omega}, f; t) + \{\mathbf{b}(\mathbf{t}) \otimes \mathbf{b}(\mathbf{t})\} \mathcal{T}_b(\boldsymbol{\Omega}, f; t) + \{\mathbf{c}(\mathbf{t}) \otimes \mathbf{c}(\mathbf{t})\} \mathcal{T}_c(\boldsymbol{\Omega}, f; t)] \quad ; \\ \mathcal{T}_a(\boldsymbol{\Omega}, f; t) &= e^{-3i\hat{f}/2} \left\{ e^{-i(\hat{f}/2)\{-2+\mathbf{a}(\mathbf{t})\cdot\boldsymbol{\Omega}\}} \text{sinc} \left[\frac{\hat{f}}{2} (1 + \mathbf{a}(\mathbf{t}) \cdot \boldsymbol{\Omega}) \right] - e^{-i(\hat{f}/2)\{2+\mathbf{a}(\mathbf{t})\cdot\boldsymbol{\Omega}\}} \text{sinc} \left[\frac{\hat{f}}{2} (1 - \mathbf{a}(\mathbf{t}) \cdot \boldsymbol{\Omega}) \right] \right\}, \\ \mathcal{T}_b(\boldsymbol{\Omega}, f; t) &= e^{-i(\hat{f}/2)[3+\{\mathbf{a}(\mathbf{t})-\mathbf{c}(\mathbf{t})\}\cdot\boldsymbol{\Omega}]} \left\{ \text{sinc} \left[\frac{\hat{f}}{2} (1 + \mathbf{b}(\mathbf{t}) \cdot \boldsymbol{\Omega}) \right] - \text{sinc} \left[\frac{\hat{f}}{2} (1 - \mathbf{b}(\mathbf{t}) \cdot \boldsymbol{\Omega}) \right] \right\}, \end{aligned}$$

$$\mathcal{T}_c(\boldsymbol{\Omega}, f; t) = e^{-3i\hat{f}/2} \left\{ e^{-i(\hat{f}/2)\{2-\mathbf{c}(t)\cdot\boldsymbol{\Omega}\}} \text{sinc} \left[\frac{\hat{f}}{2} (1 + \mathbf{c}(t) \cdot \boldsymbol{\Omega}) \right] - e^{i(\hat{f}/2)\{2+\mathbf{c}(t)\cdot\boldsymbol{\Omega}\}} \text{sinc} \left[\frac{\hat{f}}{2} (1 - \mathbf{c}(t) \cdot \boldsymbol{\Omega}) \right] \right\},$$

where the time-dependent vectors $\mathbf{a}(t)$, $\mathbf{b}(t)$ and $\mathbf{c}(t)$ represent the unit vectors pointing from the space craft 1 to 2, 2 to 3 and 3 to 1, respectively. Here, the quantity \hat{f} denotes the normalized frequency defined by

$$\hat{f} \equiv \frac{f}{f_*}; \quad f_* = 1/(2\pi L). \quad (\text{A3})$$

With the arm-length of LISA $L = 5 \times 10^6 \text{km}$, the characteristic frequency f_* becomes 9.52mHz. The analytic expressions for other detector tensors \mathbf{D}_{S_2} and \mathbf{D}_{S_3} are also obtained by the cyclic permutation of the unit vectors \mathbf{a} , \mathbf{b} and \mathbf{c} .

In the expression of antenna pattern function (A1) and/or detector tensor, the time-dependence is incorporated through the unit vectors $\mathbf{a}(t)$, $\mathbf{b}(t)$ and $\mathbf{c}(t)$, which are determined by the orbital motion of LISA. Assuming the rigid motion in the equal-arm length limit, these are given by⁴

$$\begin{pmatrix} \mathbf{a}(t) \\ \mathbf{b}(t) \\ \mathbf{c}(t) \end{pmatrix} = \mathbf{R}_z(-\phi_D(t)) \cdot \mathbf{R}_y(-\theta_D) \cdot \mathbf{R}_z(\phi_D(t)) \cdot \begin{pmatrix} \mathbf{a}_0 \\ \mathbf{b}_0 \\ \mathbf{c}_0 \end{pmatrix}. \quad (\text{A4})$$

Here the quantities \mathbf{R}_y and \mathbf{R}_z are respectively the 3×3 rotation matrices around y - and z -axes defined in the ecliptic coordinate system (see Fig.1 of paper I). The angles ϕ_D and θ_D are chosen as $\phi_D = -\pi + \omega_{\text{orbit}} t$ and $\theta_D = -\pi/3$. The vectors \mathbf{a}_0 , \mathbf{b}_0 and \mathbf{c}_0 represent the orientation of LISA in detector's rest frame. Here, we specifically set

$$\mathbf{a}_0 = \left(-\frac{\sqrt{3}}{2}, \frac{1}{2}, 0 \right), \quad \mathbf{b}_0 = (0, -1, 0), \quad \mathbf{c}_0 = \left(\frac{\sqrt{3}}{2}, \frac{1}{2}, 0 \right). \quad (\text{A5})$$

Fig. 10 shows the intensity distribution of the antenna pattern functions at $t = 0$. The frequency is specifically chosen as $f = 3f_* \simeq 28.6 \text{mHz}$. The antenna pattern functions at high-frequency regime give a different directional response, which implies that the cross-correlation signals AE , AT and ET mutually provide an independent information about source distribution. Note that the typical angular size of the intensity patterns is roughly $30^\circ \sim 60^\circ$, which basically limits the angular resolution of the final reconstructed skymap.

Finally, the noise spectral density for each output signal is presented, which is necessary to estimate the signal-to-noise ratios. Although the optimal TDI variables are free from the noise correlations, non-vanishing contribution to the self-correlation signals does exist. The noise spectral densities for optimal TDIs are calculated as (see also [30, 40]):

$$\begin{aligned} N_A(f) &= N_E(f) = \sin^2(\hat{f}/2) \left\{ 8 \left(2 + \cos \hat{f} \right) S_{\text{shot}}(f) + 16 \left(3 + 2 \cos \hat{f} + \cos 2\hat{f} \right) S_{\text{accel}}(f) \right\}, \\ N_T(f) &= 2 \left(1 + 2 \cos \hat{f} \right)^2 \left\{ S_{\text{shot}}(f) + 4 \sin^2(\hat{f}/2) S_{\text{accel}}(f) \right\}, \end{aligned} \quad (\text{A6})$$

where the variables S_{shot} and S_{accel} represent the proof mass noise and the optical path noise, respectively. Adopting the numerical values reported in Ref.[41] (see also [40]), we obtain $S_{\text{shot}}(f) = 1.60 \times 10^{-41} \text{Hz}^{-1}$ and $S_{\text{accel}}(f) = 2.31 \times 10^{-41} (\text{mHz}/f)^4 \text{Hz}^{-1}$.

-
- [1] D. Hils, P. L. Bender, and R. F. Webbink, *Astrophys. J.* **360**, 75 (1990).
 - [2] P. L. Bender and D. Hils, *Class. Quant. Grav.* **14**, 1439 (1997).
 - [3] G. Nelemans, L. R. Yungelson, and S. F. Portegies Zwart, *Astron. Astrophys.* **375**, 890 (2001), astro-ph/0105221.
 - [4] R. Schneider, V. Ferrari, S. Matarrese, and S. F. Portegies Zwart, *Mon. Not. Roy. Astron. Soc.* **324**, 797 (2001), astro-ph/0002055.

⁴ Since we are interested in the directional information of gravitational-wave signals, only the time evolution of directional dependence is considered. Note that the inclusion of radial dependence induces the Doppler modulation of the gravitational-wave signals, which is crucial for the identification of point sources.

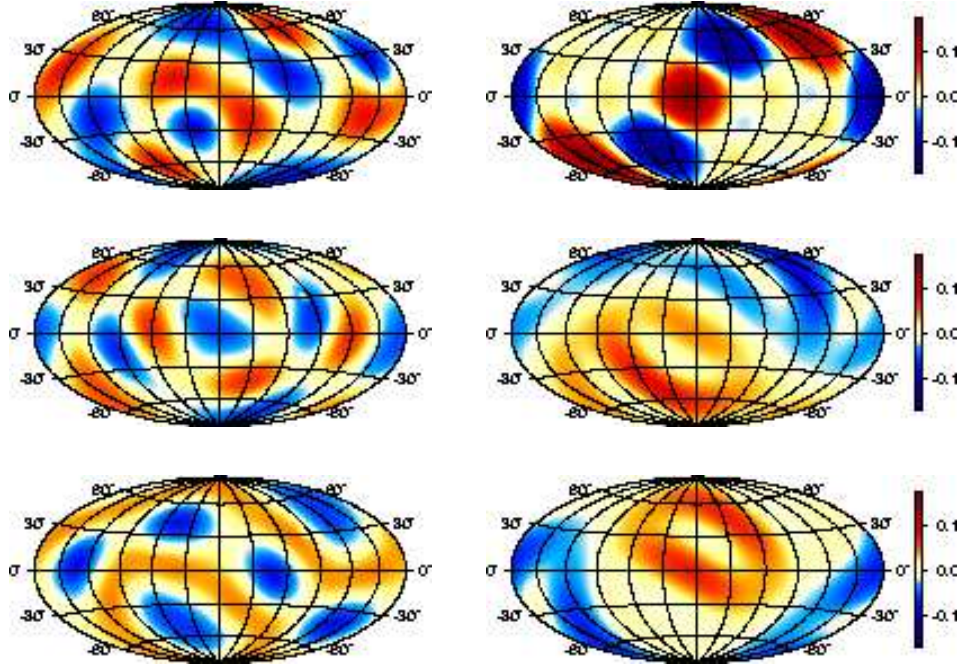


FIG. 10: Snapshots of antenna pattern functions for the cross-correlation signals AE , AT and ET at the frequency $f = 3f_* \simeq 28.6\text{MHz}$ (from top to bottom). The left and the right panels respectively show the real and the imaginary parts of the antenna pattern functions.

- [5] A. J. Farmer and E. S. Phinney, *Mon. Not. Roy. Astron. Soc.* **346**, 1197 (2003), astro-ph/0304393.
- [6] N. Seto, S. Kawamura, and T. Nakamura, *Phys. Rev. Lett.* **87**, 221103 (2001), astro-ph/0108011.
- [7] E. S. Phinney, *et al*, The Big Bang Observer: direct detection of gravitational waves from the birth of the Universe, NASA Mission Concept Study (2003).
- [8] M. S. Turner, *Phys. Rev.* **D55**, 435 (1997), astro-ph/9607066.
- [9] L. A. Boyle, P. J. Steinhardt, and N. Turok, *Phys. Rev. Lett.* **96**, 111301 (2006), astro-ph/0507455.
- [10] T. L. Smith, M. Kamionkowski, and A. Cooray, *Phys. Rev.* **D73**, 023504 (2006), astro-ph/0506422.
- [11] S. Chongchitnan and G. Efstathiou, *Phys. Rev.* **D73**, 083511 (2006), astro-ph/0602594.
- [12] C. Ungarelli, P. Corasaniti, R. A. Mercer, and A. Vecchio, *Class. Quant. Grav.* **22**, S955 (2005), astro-ph/0504294.
- [13] N. Seto, *Phys. Rev.* **D73**, 063001 (2006), gr-qc/0510067.
- [14] H. Kudoh, A. Taruya, T. Hiramatsu, and Y. Himemoto, *Phys. Rev.* **D73**, 064006 (2006), gr-qc/0511145.
- [15] H. Kudoh and A. Taruya, *Phys. Rev.* **D71**, 024025 (2005), gr-qc/0411017.
- [16] A. Taruya and H. Kudoh, *Phys. Rev.* **D72**, 104015 (2005), gr-qc/0507114.
- [17] N. Seto and A. Cooray, *Phys. Rev.* **D70**, 123005 (2004), astro-ph/0403259.
- [18] J. W. Armstrong, F. B. Estabrook, and M. Tinto, *Astrophys. J.* **527**, 814 (1999).
- [19] M. Tinto, F. B. Estabrook, and J. W. Armstrong, *Phys. Rev.* **D69**, 082001 (2004), gr-qc/0310017.
- [20] D. A. Shaddock, M. Tinto, F. B. Estabrook, and J. W. Armstrong, *Phys. Rev.* **D68**, 061303 (2003), gr-qc/0307080.
- [21] M. Tinto and S. V. Dhurandhar, *Living Rev. Rel.* **8**, 4 (2005), gr-qc/0409034.
- [22] G. Giampieri and A. G. Polnarev, *Mon. Not. R. Astron. Soc.* **291**, 149 (1997).
- [23] B. Allen and A. C. Ottewill, *Phys. Rev.* **D56**, 545 (1997), gr-qc/9607068.
- [24] N. J. Cornish, *Class. Quant. Grav.* **18**, 4277 (2001), astro-ph/0105374.
- [25] C. Ungarelli and A. Vecchio, *Phys. Rev.* **D64**, 121501 (2001), astro-ph/0106538.
- [26] N. Seto, *Phys. Rev.* **D69**, 123005 (2004), gr-qc/0403014.
- [27] W. H. Press, S. A. Teukolsky, W. T. Vetterling, and B. P. Flannery, *Numerical Recipes in Fortran 77, 2nd edition* (Cambridge University Press) (1992).
- [28] J. C. Adams and P. N. Swartztrauber, <http://www.scd.ucar.edu/css/software/spherepack/> (2003).
- [29] J. Binney, O. Gerhard, and D. Spergel, *Mon. Not. R. Astron. Soc.* **288**, 365 (1997), astro-ph/9609066.
- [30] T. A. Prince, M. Tinto, S. L. Larson, and J. W. Armstrong, *Phys. Rev.* **D66**, 122002 (2002), gr-qc/0209039.
- [31] K. R. Nayak, A. Pai, S. V. Dhurandhar, and J.-Y. Vinet, *Class. Quant. Grav.* **20**, 1217 (2003), gr-qc/0210014.
- [32] B. Allen and J. D. Romano, *Phys. Rev.* **D59**, 102001 (1999), gr-qc/9710117.
- [33] M. J. Benacquista, J. DeGoes, and D. Lunder, *Class. Quant. Grav.* **21**, S509 (2004), gr-qc/0308041.
- [34] J. A. Edlund, M. Tinto, A. Krolak, and G. Nelemans, *Phys. Rev.* **D71**, 122003 (2005), gr-qc/0504112.
- [35] S. E. Timpano, L. J. Rubbo, and N. J. Cornish, *Phys. Rev.* **D73**, 122001 (2006), gr-qc/0504071.

- [36] A. R. Thompson, J. M. Moran, and G. W. Swenson Jr., *Interferometry and Synthesis in Radio Astronomy* (Krieger Publishing Co.) (1986).
- [37] N. J. Cornish and S. L. Larson, Phys. Rev. **D67**, 103001 (2003), astro-ph/0301548.
- [38] S. D. Mohanty and R. K. Nayak, Phys. Rev. **D73**, 083006 (2006), gr-qc/0512014.
- [39] N. J. Cornish and L. J. Rubbo, Phys. Rev. **D67**, 022001 (2003), gr-qc/0209011.
- [40] N. J. Cornish, Phys. Rev. **D65**, 022004 (2002), gr-qc/0106058.
- [41] P. L. Bender and *et. al.*, LISA Pre-Phase A Report (1998).